

Advances in digital holographic micro-PTV for analyzing microscale flows

Yong-Seok Choi^{a,b}, Kyung-Won Seo^{a,b}, Myong-Hwan Sohn^{a,b}, Sang-Joon Lee^{a,b,c,*}

^a Department of Mechanical Engineering, Pohang University of Science and Technology (POSTECH), Pohang 790-784, Republic of Korea

^b Center for Biofluid and Biomimic Research, Pohang University of Science and Technology (POSTECH), Pohang 790-784, Republic of Korea

^c WCU Program Division of Integrative Biosciences and Biotechnology, Pohang University of Science and Technology (POSTECH), Pohang 790-784, Republic of Korea

ARTICLE INFO

Available online 18 July 2011

Keywords:

Digital holographic microscopy
Three-dimensional particle tracking
velocimetry (3D PTV)
Microscale flows
Biofluid flows

ABSTRACT

The accurate three-dimensional (3D) velocity field measurement technique has been receiving large attention in the study of microfluidics. DHM-PTV technique was developed by combining the digital holographic microscopy and particle tracking velocimetry technique. DHM-PTV is an ideal method for measuring three-component-three-dimensional (3C-3D) velocity field in a microscale flow with a fairly good spatial resolution. The advances in the DHM-PTV technique enable the measurement of various microscale flows, such as transport of red blood cells in a microtube and 3D flows in microfluidic devices. DHM-PTV is also applied in studying the motile behavior of swimming microorganisms. DHM-PTV would play an important role in ascertaining the undiscovered basic physics in various microscale and biofluid flow phenomena. In the current study, the basic principle of the DHM-PTV technique and its typical applications to microscale flows are introduced and discussed.

© 2011 Elsevier Ltd. All rights reserved.

1. Introduction

Recently, various microfluidic devices have been developed due to advances in micro-electromechanical systems technology [1,2]. Among these devices, bio-chips, such as μ -TAS (total analysis system) and lab-on-a-chip, are effective and efficient in early detection of diseases and use in biomedical applications. However, the development of such a bio-chip strongly requires detailed understanding of related microscale flow phenomena. Although a number of computational flow dynamics packages has been developed for studying the microfluidics phenomena, experimental observations are still important in many cases as numerical simulations are mainly focused on the validation of physical models based on observed physical phenomenon.

After Santiago et al. [3] first introduced a micro-particle image velocimetry (PIV) technique for obtaining the quantitative velocity field information of microscale flows, theoretical bases of micro-PIV measurements were established [4–11]. Nowadays, the micro-PIV technique has been applied to various microscale and biological flows. Although the conventional micro-PIV system is a relatively simple and powerful experimental tool, it has an inherent limitation of providing two-dimensional (2D) planar

velocity field information confined in a thin depth of field. The need for obtaining three-dimensional (3D) velocity field information of the flows in microfluidic devices is rapidly increasing given that the complexity of the devices is increasing as well. In addition, the 3D flow field measurement technique is strongly recommended in studying unrevealed microscale flow phenomena. A stereoscopic and a defocusing micro-PIV/PTV (particle tracking velocimetry) [12–14] were developed as 3D micro-PIV techniques. The stereoscopic system consists of two cameras for capturing two images simultaneously at slightly different viewing angles. The out-of-plane velocity component can then be extracted by relating the optical configuration and each cross-correlation map. The defocusing method involves the attaching of a mask aperture behind the lens to capture defocused particle images, which enables three-component-three-dimensional (3C-3D) velocity field measurement of microscale flows.

Holographic PIV/PTV can measure 3D velocity fields in a 3D volume of complex flows [15,16]. By adopting digital holography, several cumbersome processes can be eliminated, such as chemical and physical handlings involved in hologram reconstruction and information acquisition [17–19]. In digital holography, the hologram images of tracer particles in a flow are directly recorded using a digital image recording device, such as a charge-coupled device (CCD) or a complementary metal-oxide-semiconductor (CMOS) camera. The 3D flow information is subsequently obtained using numerical reconstruction and particle tracking procedures. However, the spatial resolution of the hologram is usually poor due to the finite size of pixels of commercial digital imaging devices. This limitation degrades the accuracy of measurement. To overcome this

* Corresponding author at: Department of Mechanical Engineering, Pohang University of Science and Technology (POSTECH), Pohang 790-784, Republic of Korea. Tel.: +82 54 279 2169; fax: +82 54 279 3199.

E-mail addresses: yschoi98@postech.ac.kr (Y.-S. Choi), kwseo@postech.ac.kr (K.-W. Seo), myongsohn@postech.ac.kr (M.-H. Sohn), sjlee@postech.ac.kr (S.-J. Lee).

pixel size limitation, the in-line digital holographic microscopy (DHM) was developed by combining in-line digital holography and optical microscopy [20–24]. The basic concept of DHM is to magnify the hologram image by employing an optical lens system so that the microscopic fringes can be resolved at a high spatial resolution. The DHM technique has been applied to microscale flows for measuring 3C–3D velocity field information using the 3D PIV/PTV algorithm [25–27].

In the current study, the basic principle of DHM-PTV and its typical applications to microscale and biological flows are briefly reviewed [28–32].

2. Digital holographic micro-particle tracking velocimetry (PTV)

Digital holography is an optical method for recording 3D volumetric field information on a digital hologram using a digital imaging device. The digital hologram is numerically reconstructed and then processed to extract 3D information. With the recent advances in in-line digital holography for analyzing fluid flows, obtaining time-resolved 3D field information by adopting a high-speed digital camera is now a possibility. The temporal evolution of 3D velocity field of a flow can be measured by applying the 3D particle tracking algorithm to the time series of holograms of particle fields.

However, the disadvantage of ‘limited spatial resolution’ is inevitable when one adopts digital imaging device to acquire the hologram. The spatial resolution of commercial digital imaging sensors is only about 100–200 line pair/mm while the holographic films are capable of 5000 line pair/mm. As a result, a limiting factor is introduced in digital holography due to the finite pixel size of the digital image sensor. The averaging effect of the pixels in recording smears the fringes having a spatial period smaller than two pixels. This leads to the following depth-of-focus of the system [19]:

$$\tau_s \approx (2\Delta)^2 / \lambda \quad (1)$$

Here Δ is the pixel size and λ is the wavelength. The value of τ_s is about several hundred micrometers in practical applications. Therefore the measurement accuracy of the digital holography is mainly limited along the direction normal to the hologram plane. The DHM technique overcomes this problem through the optical magnification of hologram images [23,33,34]. This method relieves the pixel size limitation of the image sensor array and significantly improves the spatial resolution of the digital hologram. The depth-of-focus τ_s of DHM with a magnification power M can be estimated as

$$\tau_s \approx \frac{(2\Delta/M)^2}{\lambda} \quad (2)$$

When one adopts a $20\times$ microscopic objective lens, τ_s decreases approximately 400 times compared to the conventional digital holography. Therefore in DHM, it is possible to achieve submicron accuracy along the depth-wise direction. In the following subsections, the procedures of DHM-PTV are reviewed.

2.1. Acquisition of magnified digital hologram images

Fig. 1 shows a schematic diagram of DHM-PTV. A coherent laser beam is attenuated, spatially filtered, and collimated to produce a planar reference wave. The laser beam is then scattered by particles seeded in the flow and interfered with the unaffected reference wave, generating a hologram of tracer particles. The microscope objective lens magnifies it at the imaging plane of the digital camera, which records the hologram image. The DHM-PTV

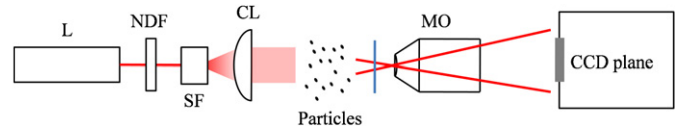


Fig. 1. Optical setup for digital holographic micro-PTV. L: laser; NDF: neutral density filter; SF: spatial filter; CL: collimating lens; and MO: microscope objective lens.

measurement can be expanded to 4D (space and time) by simply using a suitable high-speed digital camera. The recorded hologram images are then stored in the computer for digital image processing.

2.2. Pre-processing of hologram images

The eradication of background noise is essential to capture a clean hologram image. The spatially invariant background noise, such as defects in optics, can be obtained by ensemble averaging or taking pixel-by-pixel medians of consecutive hologram images. The latter method can remove the temporal as well as spatial background noise because 5–7 successive images are enough. On the other hand, the former method requires hundreds of consecutive images. The division operator was found to be the most effective in removing background noise from a raw hologram image since the intensity distribution in the image is flattened by the operation [35]. To increase further the signal-to-noise ratio of the hologram, several digital image processing techniques, including a high-pass spatial filter need to be adopted. Specifically, the use of spatial filter proved to be convenient since it can be integrated in the numerical reconstruction procedure, as described in the next subsection.

2.3. Numerical reconstruction using angular spectrum method

The reconstruction of optical field from a hologram image can be done by employing the Rayleigh–Sommerfeld diffraction theory [18,36]. As a numerical approach to the theory, the angular spectrum method is usually preferred because it does not require the minimum z -distance, which arises in the Fresnel-transform method or convolution approach [37,38]. Moreover, the angular spectrum method has the highest degree of accuracy, given that it does not require any assumptions such as the Fresnel approximation. Employing the angular spectrum method [36–38], the complex wave field reconstructed at a plane $z=d$ can be expressed as follow:

$$\Gamma(\xi, \eta; d) = \mathfrak{Z}^{-1}[\text{filter } \mathfrak{Z}\{h(x, y; 0)\} \exp(ikd\sqrt{1 - (\lambda f_x)^2 - (\lambda f_y)^2})] \quad (3)$$

where \mathfrak{Z} represents the 2D Fast Fourier transform (FFT) and *filter* indicates the filtering in the spectral domain. $h(x, y; 0)$ is the hologram function at the hologram plane $z=0$. k represents the wave number, $k = 2\pi/\lambda$. f_x and f_y are the spatial frequencies of x and y , respectively. The coordinate systems are shown in Fig. 2. In this method, the spectral filtering in frequency-domain can be easily embedded in the numerical reconstruction procedure. It is useful for blocking the direct current (DC) component and the high-frequency noises, which exceed the cutoff frequency of the system. For the calculation, only one inverse-FFT is needed at each reconstruction plane $z=d$, because the FFT of the hologram function $h(x, y; 0)$ is only required at the beginning of the reconstruction routine. Therefore this method has a fairly good computational efficiency.

The above functions need to be digitized because the hologram function is sampled on a rectangular grid of $M \times N$ points with pixel steps of Δx and Δy along the orthogonal coordinates. Here M

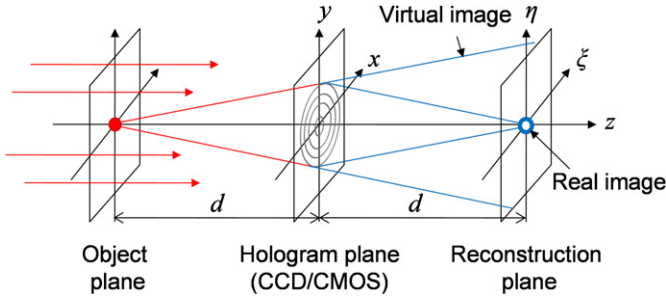


Fig. 2. Coordinate systems employed in the numerical reconstruction procedure.

and N represent the number of pixels along the row and column in the image sensor array. Using these discrete values, the spatial frequencies f_x and f_y can be calculated as follows [18]:

$$f_x = \frac{m}{M\Delta x}, \quad f_y = \frac{n}{N\Delta y} \quad (4)$$

for $m=0,1, \dots, M-1$; $n=0,1, \dots, N-1$.

Finally, Eq. (3) can be digitized as follow:

$$F(k,l;d) = \mathfrak{T}^{-1} \left[\text{filter} \mathfrak{T} \{h(m,n)\} \exp \left(ikd \sqrt{1 - \left(\frac{\lambda m}{M\Delta x} \right)^2 - \left(\frac{\lambda n}{N\Delta y} \right)^2} \right) \right] \quad (5)$$

Since the hologram image is magnified using an objective lens, the pixel steps Δx and Δy correspond to physical pixel size divided by the magnification ratio. In addition, the pixel distances in the reconstructed image are equal to those in the hologram:

$$\Delta k = \Delta x; \quad \Delta l = \Delta y \quad (6)$$

Therefore, it is more convenient to measure the volumetric flows as the reconstructed images preserve a constant scale along all coordinate directions.

It is worthwhile to note that the measurable range of DHM along the axial direction is limited by both of the pixel size and image sensor dimension of the system. For instance, the DHM system utilized in this study (wavelength $\lambda \approx 0.5 \mu\text{m}$, pixel size $\approx 10 \mu\text{m}$, image sensor size $\approx 10 \text{ mm}$, and magnification $M \approx 20$) is applicable for the ranges from several to several hundred micrometers. More detailed information on the digital holography is available in the studies of Schnars and Jüptner [18] and Meng et al. [19].

2.4. Autofocus function for precise detection of particle position

After the reconstruction process, the 3D positional information of the particles is determined from the reconstructed hologram. The in-plane (x, y) position of each particle is determined by searching the local intensity peak in the reconstructed image because the reconstructed particle has a higher intensity value than that of the background. After searching the in-plane (x, y) position, the z -position of the particle is determined. Although several techniques have been proposed, most of them exhibit poorer z -directional resolution than the in-plane precision, because the reconstructed particle images are axially elongated. The particle position along the optical axis has been mostly determined by searching for an extreme value in the reconstructed intensity, amplitude or complex variance. Therefore, such algorithms have a depth-of-focus constraint originating from the particle size [19]:

$$\tau_p \sim d^2/\lambda \quad (7)$$

where d and λ are the particle diameter and the wavelength, respectively. The quadratic dependence on the particle size makes the measurement accuracy for large particles problematic.

As we used comparably large particles in this study, a method for depth-of-focus reduction was strongly required. To solve this problem, we employed the autofocus functions, which quantify the degree of image sharpness (i.e., focus value) [29]. The focus values can be calculated by several autofocus functions defined as follows [29,39]:

$$GRA(z) = \sum_{x,y} |\nabla I(x,y;z)|, \quad (8)$$

$$SPEC(z) = \sum_{f_x, f_y} \log[1 + |\mathfrak{T}\{I(x,y;z) - \bar{I}(z)\}|], \quad (9)$$

$$LAP(z) = \sum_{x,y} \{\nabla^2 I(x,y;z)\}^2, \quad (10)$$

$$VAR(z) = \frac{1}{N_x N_y} \sum_{x,y} \{I(x,y;z) - \bar{I}(z)\}^2 \quad (11)$$

where $I(x, y; z)$ represents the intensity distribution in a segment of the reconstructed image at a depth-wise plane z . The domain of x and y coordinates is restricted to a rectangular region enclosing each particle. \bar{I} is the mean value of intensity I , and N_x and N_y are the pixel dimensions of the given segments. The above functions quantify the sharpness of reconstructed particle image for each z -position. Given that a reconstructed particle image has a maximum focus value when the reconstruction plane coincides with the actual particle position, the z -position of the particle can be determined by searching the maximum focus value [39,40]. The performance of each focus function varies according to the shape and size of the tracer particles. Therefore, choosing the best autofocus function for the given experimental condition is recommended. Fig. 3 shows typical reconstructed particle images and the corresponding focus value profile for a spherical particle of $7 \mu\text{m}$ in diameter. The focus value profile shows the maximum peak at the z -directional position where the particle image is clearly reconstructed.

The measurement accuracy of the present method was estimated by measuring the particle displacement in a laminar flow, because the velocity components perpendicular to the stream-wise (x) direction are negligible in the flow. The resultant root

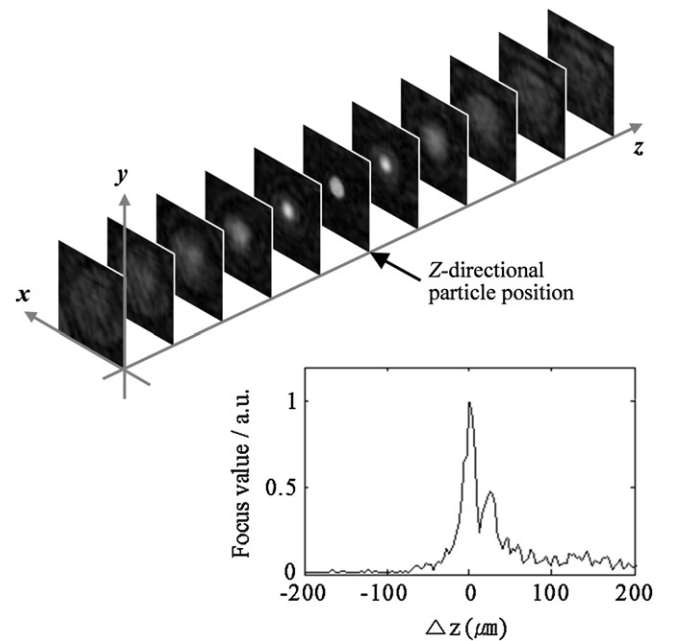


Fig. 3. Reconstructed particle images and the corresponding focus value profile for a spherical particle of $7 \mu\text{m}$ in diameter.

Table 1

RMS measurement errors (ε) along the lateral (x, y) and axial (z) directions with respect to the particle diameter (d).

d (μm)	7.0	15.0	30.1
$\varepsilon_{\text{lateral}}$ (μm)	0.24 (0.03 d)	0.36 (0.02 d)	0.62 (0.02 d)
$\varepsilon_{\text{axial}}$ (μm)	1.51 (0.22 d)	2.96 (0.20 d)	5.68 (0.19 d)

mean square (RMS) displacements of the particles along the lateral (x, y) and axial (z) directions are summarized in Table 1. The measurement uncertainty in the axial direction is nearly one order larger than those in the lateral directions. The uncertainty for velocity measurement is directly related to the error of displacement measurement. Hence the measurement uncertainty for the velocity in the axial direction would also be one order larger than those in the lateral directions. This is mainly attributed to the inherent shortcoming of the in-line digital holography technique. It is worthwhile to note that the measurement uncertainty also depends on the particle size.

2.5. Three-dimensional particle tracking velocimetry (3D PTV) algorithm

The trajectory of a reconstructed particle can be obtained by applying PTV algorithms to the successively extracted positional information of the particle [41–44]. The two-frame PTV algorithm based on match probability for successive particle tracking [41] is employed. This PTV algorithm utilizes the heuristics corresponding to the maximum displacement limit, small velocity change, common motion, and consistent match between two successive frames captured within a time interval Δt . After matching the same particles in two consecutive particle sets, the velocity information is determined by dividing the displacement vectors with the time interval Δt . By repeating the particle tracking process for whole particle sets, the trajectory information of each particle can be obtained.

3. Applications to various microscale flows

The newly developed DHM-PTV technique is applied to several microscale flows. First, the 3D motion of red blood cells (RBCs) in a microtube flow is tracked using DHM-PTV [29]. Then, the radial focusing of spherical particles due to inertial migration is observed in a microtube and a microchannel at moderate Reynolds numbers [30,31]. Finally, the 3D motility of swimming microorganisms is analyzed using the DHM-PTV technique [32].

3.1. 3D tracking of red blood cells in a microtube flow

Recently, the hemodynamic information of blood flows has been receiving much attention due to the rapid increase in the occurrence of circulatory vascular diseases. In the present study, 3D trajectories and velocity fields of RBCs flowing in a microtube are measured using the DHM-PTV technique. The experimental apparatus consists of a He–Ne laser, a spatial filter, a water-immersion objective lens ($\times 20$), and a high-speed digital camera. The RBC suspension diluted to a hematocrit of Hct=0.05% is supplied to an FEP microtube ($D=350\ \mu\text{m}$) immersed in water. Given that the refractive indices of the solution (plasma, $n=1.346$), FEP tube ($n=1.338$), and water ($n=1.333$) are similar, the refractive distortion in the hologram image is prevented.

Fig. 4a–d shows a typical hologram image of RBCs and reconstructed images at three selected depth planes. In each reconstruction image, some RBCs are clearly observed in good focus. In the region near the bottom wall, the number of focused

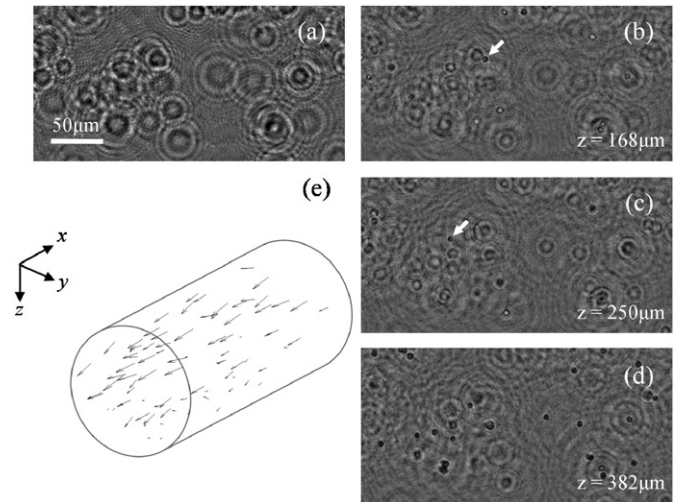


Fig. 4. (a) Typical hologram of RBCs in a microtube flow; (b–d) reconstructed images at three selected depth planes wherein each focused RBC is marked by an arrow; and (e) 3D instantaneous velocity vectors of RBCs obtained from two consecutive holograms.

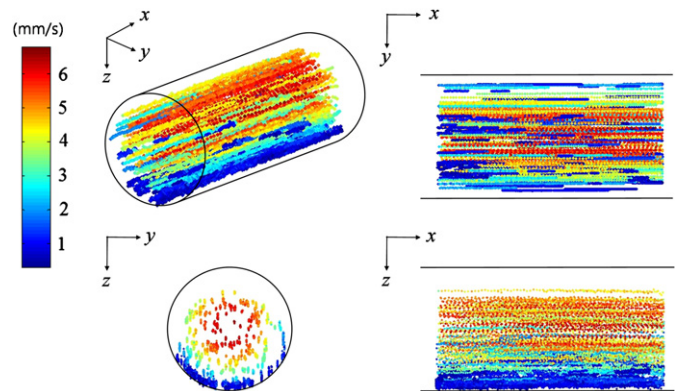


Fig. 5. Trajectories of RBCs in a microtube flow. Color indicates the streamwise velocity of RBCs.

RBCs is increased because the density of RBC ($\rho=1.095$) is slightly higher than that of the blood plasma ($\rho=1.027$). Fig. 4e illustrates the instantaneous vectors of RBCs in the microtube flow. The 4D (x, y, z, t) trajectories of tracked RBCs are shown in Fig. 5. The trajectories of RBCs clearly indicate their linear movement. The velocity profile of RBCs is in good agreement with the Poiseuille velocity profile. Although some fluctuations are observed along the z -direction, the 3D motion of RBCs can be tracked with reasonable accuracy.

3.2. Inertial migration of microspheres in microtube and microchannel flows

The inertial migration of particles in a Poiseuille flow can be utilized for practical applications, such as the passive separation or alignment of particles [45,46]. The particles suspended in a Poiseuille flow tend to migrate across streamlines toward the equilibrium position at approximately 0.6 radii by the force balance between wall repulsion and inertial lift. In an axisymmetric Poiseuille pipe flow, the equilibrium position appears as a ring shape called the Segré–Silberberg annulus [47]. On the contrary, there are four equilibrium positions near the center of each face in a square microchannel [48]. In the current study, the

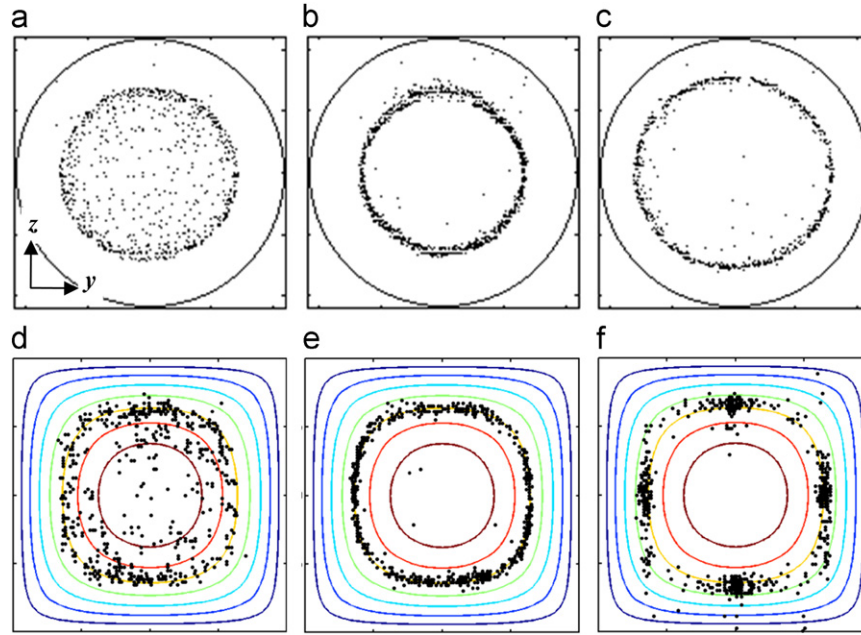


Fig. 6. Spatial distribution of particles over a cross-sectional plane in a microtube and a microchannel. (a) $a/H=0.04$, $Re=9.7$, (b) $a/H=0.08$, $Re=9.7$, (c) $a/H=0.04$, $Re=77.4$, (d) $a/H=0.16$, $Re=7.1$, (e) $a/H=0.16$, $Re=12$, and (f) $a/H=0.16$, $Re=120$.

3D positions of particles suspended in a microtube and in a square microchannel are measured using DHM-PTV.

The experimental setup consists of a continuous Nd:YAG laser, a water-immersion objective lens ($\times 20$), and a digital CMOS camera. The testing fluid is injected into the microtube ($D=350\ \mu\text{m}$, $L=300\ \text{mm}$) or the microchannel ($H=100\ \mu\text{m}$, $L=100\ \text{mm}$) using a syringe pump. Polystyrene microspheres ($\rho_p=1.05\ \text{g cm}^{-3}$) with mean diameters of $a=7\text{--}30\ \mu\text{m}$ are mixed at a dilution of 0.05% w/v with water. The density of water is carefully matched with that of the particles by dissolving sodium chloride to attain neutral buoyancy. The Reynolds number $Re=U_m H/\nu$ is in the range $Re=4.7\text{--}120$, where U_m is the maximum flow velocity, H is the hydraulic diameter, and ν is the kinematic viscosity. The ratios of the particle diameter to the hydraulic diameter are $a/H=0.04\text{--}0.16$.

From each of the hologram image, the 3D positional information of the particles are extracted and superimposed onto a cross-sectional (y, z) plane of the conduits to get the spatial distribution of the particles. Fig. 6 shows the obtained spatial distributions of the particles in the two flows. As shown in Fig. 6a–c, the tubular pinch effect of the particles is significant at a certain radial position, and the Segré–Silberberg annulus becomes obvious with increasing particle size and Re in microtube flow. Fig. 6d–f illustrates the spatial distribution of particles in a square microchannel. As Re increases, the outward lateral migration in the central region becomes prevalent and a focused particle annulus is formed at a certain lateral position (Fig. 6e). As Re is further increased, the particles begin to migrate cross-laterally toward the four equilibrium positions located near the center of each face (Fig. 6f). Along these lines, future investigations related to the transport of particles in microscale channel flows have to consider the nonlinear hydrodynamic phenomena, that is, inertial migration.

3.3. Analysis of 3D motile characteristics of swimming microorganisms

Majority of the previous studies on motile characteristics of microorganisms has been performed using numerical simulation or 2D measurements [49,50]. However, most microorganisms, such as flagellates, ciliates, and motile germ cells, inherently

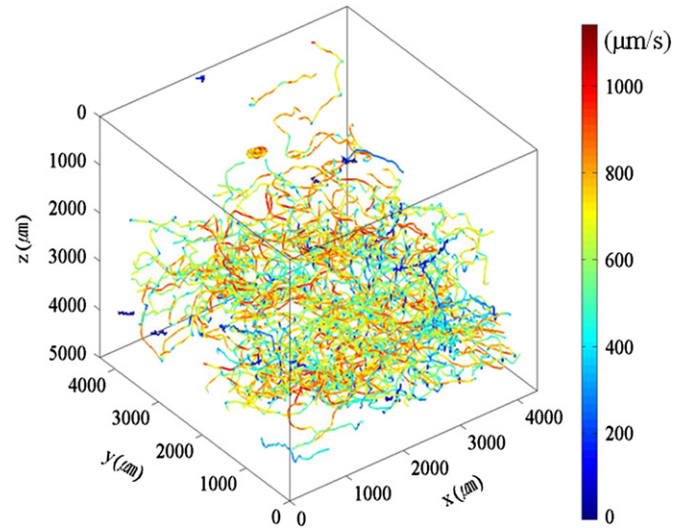


Fig. 7. Three-dimensional trajectories of free-swimming *C. Polykrikoides* with color-coded speed.

exhibit 3D swimming features [51]. Therefore, to understand the motile behaviors of microorganisms in detail, accurate measurement of their 3D motions is strongly recommended. Recently, the digital holographic PTV technique has been employed in observing the 3D motion of microorganisms and in measuring the velocity fields induced by them [25,52,53].

In the present study, the 3D free-swimming motion of *Cochlodinium polykrikoides*, a phytoplankton species that causes red tide, is measured using the DHM-PTV technique with a high depth-directional accuracy [32]. *C. polykrikoides* usually forms chains in the exponential and stationary growth phases. The chain-forming cells consist of 2, 4, 8, and, occasionally, 16 cells. A single *C. polykrikoides* cell has an ellipsoidal shape, with a length of $30\text{--}40\ \mu\text{m}$ and a width of $25\text{--}30\ \mu\text{m}$. The sample chamber is made of BK7 glass windows with dimensions of $10 \times 10 \times 5\ \text{mm}^3$. The size of the chamber is large enough for the cells to swim

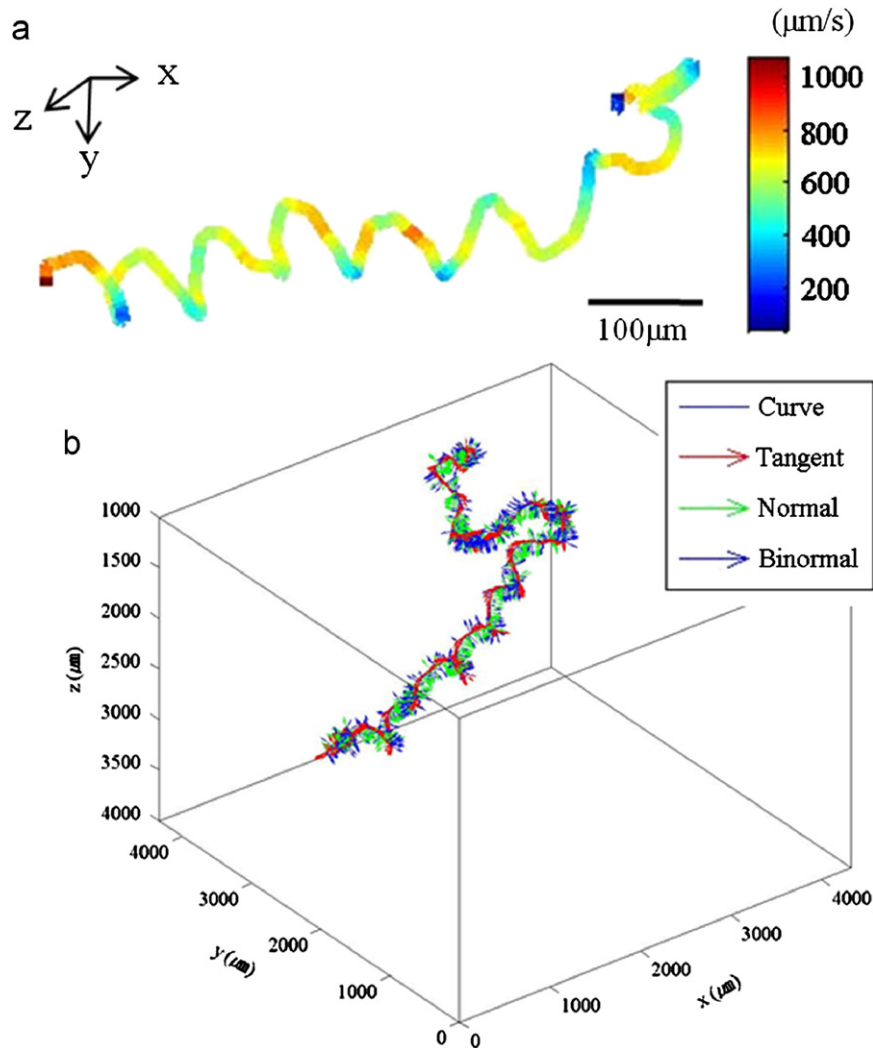


Fig. 8. (a) Representative helical swimming trajectory of a 4-cell *C. polykrikoides* chain; (b) orientation variation of a swimming microorganism compared to their trajectories and helices.

freely. A collimated He–Ne laser beam is used to illuminate the cells in the sample chamber. To magnify the hologram images, an objective lens ($\times 4$) is attached in front of the high-speed CMOS camera. The field of view is $4.3 \times 4.3 \times 5 \text{ mm}^3$ with a spatial resolution of approximately $4.2 \mu\text{m}$ in the lateral direction.

Fig. 7 shows the 3D swimming trajectories of several hundred *C. polykrikoides* cells with color-coded speed. The average swimming speed for solitary cells is $391 \pm 92 \mu\text{m s}^{-1}$. For the 2-, 4-, and 8-cell chains, the average swimming speeds are 599 ± 126 , 800 ± 129 , and $856 \pm 108 \mu\text{m s}^{-1}$, respectively. On the average, the chain-forming cells have faster swimming speeds than solitary cells. This can be explained by assuming that the hydrodynamic drag of chain-forming cells is the Stokes drag of a prolate-spheroid body shape. As the cells form a chain, the total drag is dramatically decreased compared with the sum of drags of solitary cells. Apart from the swimming trajectories and moving speed, the swimming attitude, orientations, and helices can be extracted as shown in Fig. 8. As the number of cells in a chain increases, the helix radius and pitch increase.

4. Concluding remarks

Due to the advances in optics, laser, computer, and digital image processing techniques, digital holography becomes an

essential tool for 3D measurements. In addition, the DHM-PTV technique is an ideal method for measuring 3C-3D velocity field information of a microscale flow with a fairly good spatial resolution. Moreover, the cost required to develop a DHM-PTV system is approximately as much as the price of a conventional micro-PIV system because both of them are composed of similar optical components.

As briefly reviewed in this paper, the advances in the DHM-PTV technique will enable the measurement of various microscale flows in which 3D flow analysis is indispensable, such as in measuring the transport of biological fluids in microvascular vessels and 3D flows in various microfluidic devices. DHM-PTV would play an important role in revealing the undiscovered basic physics of various microscale flow phenomena.

Acknowledgment

This work was supported by the Creative Research Initiatives (Diagnosis of Biofluid Flow Phenomena and Biomimetics Research) of MEST/KOSEF, the World-Class University program through the National Research Foundation of Korea, and funded by the Ministry of Education, Science, and Technology (R31-2008-000-10105-0).

References

- [1] Gravesen P, Branebjerg J, Jensen OS. Microfluidics—a review. *J Micromech Microeng* 1993;3:168–82.
- [2] Stone HA, Stroock AD, Ajdari A. Engineering flows in small devices: microfluidics toward a lab-on-a-chip. *Annu Rev Fluid Mech* 2004;36:381–411.
- [3] Santiago JG, Wereley ST, Meinhart CD, Beebe DJ, Adrian RJ. A particle image velocimetry system for microfluidics. *Exp Fluids* 1998;25:316–9.
- [4] Meinhart CD, Wereley ST, Santiago JG. PIV measurements of a microchannel flow. *Exp Fluids* 1999;27:414–9.
- [5] Meinhart CD, Wereley ST, Gray MHB. Volume illumination for two-dimensional particle image velocimetry. *Meas Sci Technol* 2000;11:809–14.
- [6] Meinhart CD, Wereley ST, Santiago JG. A PIV algorithm for estimating time-averaged velocity fields. *J Fluids Eng* 2000;122:285–9.
- [7] Meinhart CD, Wereley ST. The theory of diffraction-limited resolution in microparticle image velocimetry. *Meas Sci Technol* 2003;14:1047–53.
- [8] Olsen MG, Adrian RJ. Out-of-focus effects on particle image visibility and correlation in microscopic particle image velocimetry. *Exp Fluids* 2000;7: S166–74.
- [9] Olsen MG, Adrian RJ. Brownian motion and correlation in particle image velocimetry. *Opt Laser Technol* 2000;32:621–7.
- [10] Olsen MG, Bourdon CJ. Out-of-plane motion effects in microscopic particle image velocimetry. *J Fluids Eng* 2003;125:895–901.
- [11] Wereley ST, Gui L, Meinhart CD. Advanced algorithms for microscale particle image velocimetry. *AIAA J* 2002;40:1047–55.
- [12] Brown MR, MacInnes JM, Allen RWK, Zimmerman WBJ. Three-dimensional, three-component velocity measurements using stereoscopic micro-PIV and PTV. *Meas Sci Technol* 2006;17:2175–85.
- [13] Kajitani L, Dabiri D. A full three-dimensional characterization of defocusing digital particle image velocimetry. *Meas Sci Technol* 2005;16:790–804.
- [14] Yoon SY, Kim KC. 3D particle position and 3D velocity field measurement in a microvolume via the defocusing concept. *Meas Sci Technol* 2006;17: 2897–905.
- [15] Meng H, Hussain F. In-line recording and off-axis viewing technique for holographic particle velocimetry. *Appl Opt* 1995;34:1827–40.
- [16] Sheng J, Malkiel E, Katz J. Single beam two-views holographic particle image velocimetry. *Appl Opt* 2003;42:235–50.
- [17] Schnars U, Jüptner W. Direct recording of holograms by a CCD target and numerical reconstruction. *Appl Opt* 1994;33:179–81.
- [18] Schnars U, Jüptner W. *Digital Holography*. Berlin: Springer; 2005.
- [19] Meng H, Pan G, Pu Y, Woodward SH. Holographic particle image velocimetry: from film to digital recording. *Meas Sci Technol* 2004;15:673–85.
- [20] Xu W, Jericho MH, Meinertzhagen IA, Kreuzer HJ. Digital in-line holography of microspheres. *Appl Opt* 2002;41:5367–75.
- [21] Satake S, Kunugi T, Sato K, Ito T, Taniguchi J. Three-dimensional flow tracking in a micro channel with high time resolution using micro digital-holographic particle-tracking velocimetry. *Opt Rev* 2005;12:442–4.
- [22] Satake S, Kunugi T, Sato K, Ito T, Kanamori H, Taniguchi J. Measurements of 3D flow in a micro-pipe via micro digital holographic particle tracking velocimetry. *Meas Sci Technol* 2006;17:1647–51.
- [23] Sheng J, Malkiel E, Katz J. Digital holographic microscope for measuring three-dimensional particle distributions and motions. *Appl Opt* 2006;45: 3893–901.
- [24] Kim S, Lee SJ. Measurement of 3D laminar flow inside a micro tube using micro digital holographic particle tracking velocimetry. *J Micromech Microeng* 2007;17:2157–62.
- [25] Sheng J, Malkiel E, Katz J, Adolf J, Belas R, Place AR. Digital holographic microscopy reveals prey-induced changes in swimming behavior of predatory dinoflagellates. *Proc Natl Acad Sci USA* 2008;104:17512–7.
- [26] Sheng J, Malkiel E, Katz J. Using digital holographic microscopy for simultaneous measurements of 3D near wall velocity and wall shear stress in a turbulent boundary layer. *Exp Fluids* 2008;45:1023–35.
- [27] Ooms TA, Lindken R, Westerweel J. Digital holographic microscopy applied to measurement of a flow in a T-shaped micromixer. *Exp Fluids* 2009;47: 941–55.
- [28] Kim S, Lee SJ. Measurement of Dean flow in a curved micro-tube using micro digital holographic particle tracking velocimetry. *Exp Fluids* 2009;46: 255–64.
- [29] Choi YS, Lee SJ. Three-dimensional volumetric measurement of red blood cell motion using digital holographic microscopy. *Appl Opt* 2009;48:2983–90.
- [30] Choi YS, Lee SJ. Holographic analysis of three-dimensional inertial migration of spherical particles in micro-scale pipe flow. *Microfluid Nanofluid* 2010;9:819–29.
- [31] Choi YS, Seo KW, Lee SJ. Lateral and cross-lateral focusing of spherical particles in a square microchannel. *Lab Chip* 2011;11:460–5.
- [32] Sohn MH, Seo KW, Choi YS, Lee SJ, Kang YS, Kang YS. Determination of the swimming trajectory and speed of chain-forming dinoflagellate *Cochlodinium polykrikoides* with digital holographic particle tracking velocimetry. *Mar Biol* 2011;158:561–70.
- [33] Kemper B, Carl D, Knoche S, Thien R, von Bally G. Holographic interferometric microscopy systems for the application on biological samples. *Proc SPIE* 2004;5457:581–9.
- [34] Carl D, Kemper B, Wernicke G, von Bally G. Parameter optimized digital holographic microscope for high resolution living cell analysis. *Appl Opt* 2004;43:6536–44.
- [35] Jacob PF, Timothy JS, Raymond AS. Practical methods for automated reconstruction and characterization of particles in digital in-line holograms. *Meas Sci Technol* 2009;20:075501.
- [36] Goodman JW. *Introduction to Fourier optics*. second ed. New York: McGraw-Hill; 1996.
- [37] Kim MK, Yu L, Christopher JM. Interference techniques in digital holography. *J Opt A: Pure Appl Opt* 2006;8:S518–23.
- [38] Yu L, Kim MK. Wavelength-scanning digital interference holography for tomographic 3D imaging using the angular spectrum method. *Opt Lett* 2005;30:2092–4.
- [39] Langehanenberg P, Kemper B, Dirksen D, Bally GV. Autofocusing in digital holographic phase contrast microscopy on pure phase objects for live cell imaging. *Appl Opt* 2008;47:D176–82.
- [40] Groen FC, Young IT, Lighthart G. A comparison of different focus functions for use in autofocus algorithms. *Cytometry* 1985;6:81–91.
- [41] Baek SJ, Lee SJ. A new two-frame particle tracking algorithm using match probability. *Exp Fluids* 1996;22:23–32.
- [42] Crocker JC, Grier DG. Methods of digital video microscopy for colloidal studies. *J Colloid Interface Sci* 1996;179:298–310.
- [43] Sheng J, Meng H. A genetic algorithm particle pairing technique for 3D velocity field extraction in holographic particle image velocimetry. *Exp Fluids* 1998;25:461–73.
- [44] Krepli R, Pu Y, Meng H, Obermayer K. A new algorithm for the interrogation of 3D holographic PTV data based on deterministic annealing and expectation minimization optimization. *Exp Fluids* 2000;29:S99–107.
- [45] Bhagat AAS, Kuntaegowdanahalli SS, Papautsky I. Inertial microfluidics for continuous particle filtration and extraction. *Microfluid Nanofluid* 2009;7: 217–26.
- [46] Di Carlo D, Irimia D, Tompkins RG, Toner M. Continuous inertial focusing, ordering, and separation of particles in microchannels. *Proc Natl Acad Sci USA* 2007;104:18892–7.
- [47] Segré G, Silberberg A. Radial particle displacements in Poiseuille flow of suspensions. *Nature* 1961;189:209–10.
- [48] Di Carlo D, Edd JF, Humphry KJ, Stone HA, Toner M. Particle segregation and dynamics in confined flows. *Phys Rev Lett* 2009;102:094503.
- [49] Kamykowski D, Reed RE, Kirkpatrick GJ. Comparison of sinking velocity, swimming velocity, rotation and path characteristics among six marine dinoflagellate species. *Mar Biol* 1992;113:319–28.
- [50] Miyasaka I, Nanba K, Furuya K, Nimura Y, Azuma A. Functional roles of the transverse and longitudinal flagella in the swimming motility of *Prorocentrum minimum* (Dinophyceae). *J Exp Biol* 2004;207:3055–66.
- [51] Crenshaw HC. Orientation by helical motion-kinematics of the helical motion of organisms with up to six degrees of freedom. *Bull Math Biol* 1993;55: 197–212.
- [52] Heydt M, Rosenhahn A, Grunze M, Pettitt M, Callow ME, Callow JA. Digital in-line holography as a three-dimensional tool to study motile marine organisms during their exploration of surfaces. *J Adhes* 2007;83:417–30.
- [53] Lewis NI, Xu W, Jericho SK, Kreuzer HJ, Jericho MH, Cembella AD. Swimming speed of three species of Alexandrium (Dinophyceae) as determined by digital in-line holography. *Phycologia* 2006;45:61–70.